Multiphase Phenomena and CFD Modeling and Simulation in Materials Processes
Edited by Laurentiu Nastac and Ben Q. Li TMS (The Minerals, Metals & Materials Society), 2004

On convection-induced phase separation during solidification

Andreas Ludwig, Menghuai Wu, Sven Eck

Simulation and Modeling of Metallurgical Processes, University of Leoben
Franz-Josef-Str. 18; A- 8700 Leoben, Austria

Keywords: Modeling, solidification, phase separation, simulation, casting

Abstract

Phase separation is a frequently occurring phenomenon during solidification accompanied by melt convection, sedimentation or, in the case of two unmixable liquids, a Marangoni driven motion. In order to describe these phase separation phenomena a two-phase volume-averaging model was employed for globular equiaxed solidification of binary alloys and decomposition and solidification of hypermonotectic alloys. The model considers nucleation and growth of equiaxed grains or second phase droplets, motion and sedimentation of grains or droplets, feeding flow and solute transport by diffusion and convection. It allows the prediction of macro segregations and the distributions of grain size or droplet size. Evaluations were made by comparing the numerical predictions with experimental results. For example it is shown that the numerically predicted grain size distribution in a plate casting (Al-4wt%Cu) agrees reasonably well with the experimental analyses.

Introduction

Modeling of metallurgical processes is a rapidly expanding field and the research activities in the last decades cover a wide range of areas including melt pre-treatment, solidification and subsequent manufacturing routes. Among those activities solidification stands in the central position, because the primary structure of the materials, and even many defects such as porosity, (macro or micro) segregation and inclusions form during solidification. Those primarily formed structures or defects once existing are difficult to be removed or modified by the subsequent material processing.

Solidification is a multi-disciplinary field involving thermodynamics, fluid dynamics and solid mechanics, heat and mass transfer, and other disciplines[1-3]. One of the most challenging problems in solidification modeling is the complex interactions between physical phenomena occurring on different length scales ranging from atomic rearrangement over single crystal-melt interactions to heat extraction, momentum and species transport at the system level. Modeling an industry process on atomic scale is unrealistic, even on grain scale (e.g. phase field method) it would need another 40 years to be able to model the exact grain morphology in a casting space envelope of 10x10x10 cm^3 [4]. Therefore, the realistic models for industry process are based on the solution of the macro transport equations (mass, momentum, enthalpy and species) on system scale. The microscopic phenomena such as thermodynamics, nucleation law, crystal growth kinetics and interactions at the liquid-solid interface are considered with simplified models, which are coupled with the macroscopic transport equations.

The single-phase solidification model has undergone a significant development in the last decades. Some commercial software (e.g. MAGMASOFT and ProCAST) has been to some extent applied to industry for mold filling and solidification of shape castings. The shortage of the single-phase model is obvious. It is widely accepted that there are (at least) two phases

coexisted during solidification, namely the liquid and the solid (see Figure1). Both phases have different properties and different concentrations, and they behave in different ways. It is not possible to describe the solidification process of Figure 1 with a single-phase model adequately.

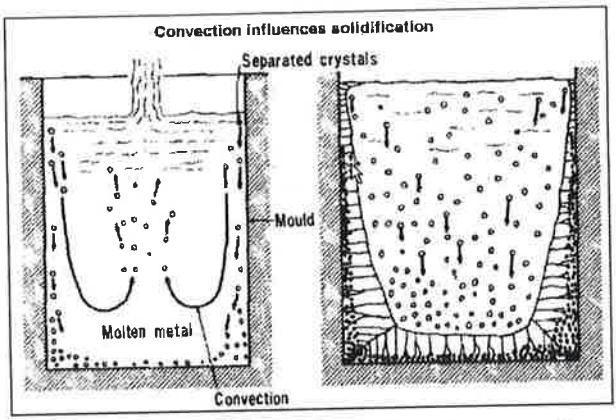

Figure 1: Schematic show of the solidification process[5]

A multi-phase model based on the volume-averaging theorem was developed first by Beckermann's group[1,6-12]. They treated the liquid and solid as separate interpenetrating continua, established and solved the transport equations (mass, momentum, energy and solute) for the liquid and solid simultaneously. In this way they permitted a rigorous description of disparate solid and liquid velocities, interactions, thermal and constitutional non-equilibrium, and many other microscopic phenomena. However, this pioneering model involves many uncertainties[13,14], e.g. the lack of a realistic nucleation model, detailed volumetric heat and mass transfer coefficients (or thermal and solute diffusion lengths), correct stereological formations for interfacial area concentration, etc. A good deal of additional research is needed before the advantages of Beckermann's model may be fully explored[1,11,15]. Therefore, this multi-phase approach has been further modified (simplified) by Ludwig and co-workers[16-26], and it has been applied to globular equiaxed solidification in industry alloys and phase separation phenomenon in hypermonotectic alloys.

Model description

In the multiphase model the different phases are treated mathematically as interpenetrating continua. The phases can be liquids, solids or gases. Since the volume of a phase cannot be occupied by other phases, the concept of phasic volume fraction is introduced. These volume fractions, α_q, are assumed to be continuous functions of space and time and their sum is equal to one:

$$\sum_{q=1}^{\vec{n}} \alpha_q = 1, \tag{1}$$

n is the number of phases, q is the phase index. The multiphase model solves a set of n momenta, enthalpies and continuities and m species for each phase. Coupling is achieved through the pressure (one pressure field for all phases) and interphase exchange terms. The solution procedure to the conservation equations is performed with the help of the commercial software FLUENT in the Eulerian multiphase module. The capability of user-defined

subroutines (UDS) allows customisation of the momentum exchange, species, and heat exchange, etc. The user-defined scalar functions allow customisation of additional conservation equations.

Conservation equations

The description of the multiphase conservations by conservation equations follows the lines of the FLUENT manual[28]

Mass conservation (continuity equation)
The continuity equation for phase q is

$$\frac{\partial}{\partial t}\alpha_q\rho_q + \nabla\cdot\alpha_q\rho_q\vec{u}_q = \sum_{p=1}^{\vec{n}}\dot{m}_{pq}\,, \tag{2}$$

where ρ_q and $\vec{u}_q$ are the density and the velocity of the phase q, respectively. $\dot{m}_{pq}$ is the mass transfer from phase p to phase q. It subjects $\dot{m}_{pq} = -\dot{m}_{qp}$.

Momentum conservation (Navier-Stokes)

$$\frac{\partial}{\partial t}\left(\alpha_q\rho_q\vec{u}_q\right) + \nabla\cdot\left(\alpha_q\rho_q\vec{u}_q\otimes\vec{u}_q\right) = -\alpha_q\nabla p + \nabla\cdot\bar{\bar{\tau}}_q + \vec{F}_M + \sum_{p=1}^{\vec{n}}K_{pq}\left(\vec{u}_p - \vec{u}_q\right) + \sum_{p=1}^{\vec{n}}\dot{m}_{pq}\vec{u}_{pq}\,, \tag{3}$$

where $\bar{\bar{\tau}}_q$ is the stress-strain tensor of phase q:

$$\bar{\bar{\tau}}_q = \alpha_q\mu_q\left(\nabla\vec{u}_q + \left(\nabla\vec{u}_q\right)^T\right) + \alpha_q\left(\lambda_q - \frac{2}{3}\mu_q\right)\nabla\cdot\vec{u}_q\bar{\bar{I}} \tag{4}$$

Here μ_q and λ_q are the shear and bulk viscosity of phase q, $\vec{F}_M$ is Marangoni force in case of monotectic solidification, $\otimes$ is a dyadic product, and p in the equation (not as subscript) is the pressure shared by all phases. $\vec{u}_{pq}$ is the interphase velocity, defined as follows. If $\dot{m}_{pq} > 0$ (i.e., phase p mass is being transferred to phase q), then $\vec{u}_{pq} = \vec{u}_p$; if $\dot{m}_{pq} < 0$ (i.e., phase q mass is being transferred to phase p), then $\vec{u}_{pq} = \vec{u}_q$; and $\vec{u}_{pq} = \vec{u}_{qp}$.
$K_{pq}(=K_{qp})$ is the interphase momentum exchange coefficient, depending on the friction, pressure, cohesion and other effects.

Energy (enthalpy) conservation

$$\frac{\partial}{\partial t}\left(\alpha_q\rho_q h_q\right) + \nabla\cdot\left(\alpha_q\rho_q\vec{u}_q h_q\right) = \alpha_q\frac{dp_q}{dt} + \bar{\bar{\tau}}_q : \nabla\vec{u}_q - \nabla\cdot\vec{q}_q + S_q + \sum_{p=1}^{n}\left(Q_{pq} + \dot{m}_{pq}h_{pq}\right), \tag{5}$$

where h_q is the specific enthalpy of phase q, which is defined as

$$h_q = \int_{T_{ref}}^{T_q} c_{p(q)}\,dT_q + h_q^{ref}\,, \tag{6}$$

$c_{p(q)}$ is the specific heat of phase q, h_q^{ref} is the enthalpy at the reference temperature T_{ref}. In equation (5), $\bar{q}_q$ is the heat flux, S_q is a source term that includes sources of enthalpy (e.g. due to chemical reaction or radiation), Q_{pq} is the intensity of heat exchange between the phases p and q, and h_{pq} is the interphase enthalpy (e.g. the latent heat in case of phase transition). The heat exchange between the phases must comply with the local balance conditions $Q_{pq} = -Q_{qp}$ and $Q_{qq} = 0$.

Species (concentration) conservation
The closure of the equation set is completed by conservation equations describing the mass fraction of the species i in the phase q:

$$\frac{\partial}{\partial t}\left(\alpha_q \rho_q m_q^i\right) + \nabla \cdot \left(\alpha_q \rho_q \bar{u}_q m_q^i\right) = \nabla \cdot \left(\alpha_q \rho_q D_q^i \nabla m_q^i\right) + \dot{m}_q^i, \tag{7}$$

where m_q^i is the mass fraction of the species i in the phase q, D_q^i is the diffusivity of the species i in the mixture of the phase q, and $\dot{m}_q^i$ is the rate of production/destruction of the species i.

User-Defined Scalar transport equations
It is possible to solve the transport equations for arbitrary scalars in the same way as the transport equation for enthalpy. For example, the grain density of equiaxed solidification[18] and the drop density of the secondary liquid phase in monotectic solidification[23] were modeled with an additional scalar transport equation.
The general form of the arbitrary scalar $_k$ is

$$\frac{\partial \rho_{\ k}}{\partial t} + \frac{\partial}{\partial x_i}\left(\rho \bar{u}_{i\ k} - \Gamma_k \frac{\partial\ _k}{\partial x_i}\right) = S_{\ k}, \tag{8}$$

where Γ_k and $S_{\ k}$ are the diffusion coefficient and source term for each of the N scalar equations.

Source terms and interaction terms

Whether the Eulerian multiphase model will be successfully applied to the solidification and phase separation processes is strongly dependent on the definition and implementation (through user defined subroutines) of source terms, interaction terms, and other auxiliary terms into the conservation equations. Previous works have demonstrated how to apply those terms into conservation equations and how to model multi-phase solidification problems[16-26]. A brief description is given below.

Nucleation and transport of moving grains (or droplets) during solidification
The idea for modeling the grain density during globular equiaxed solidification (or droplet density during hypermonotectic solidification) is to define a user-defined-scalar function n, which can be estimated by solving the conservation equation

$$\frac{\partial}{\partial t} n + \nabla \cdot (\vec{u}_q n) = N \,, \tag{9}$$

where n is the grain or droplet density. Equation (9) is derived from equation (8), by ignoring the diffusion (Γ) of the scalar function. N (number of grains nucleated per volume and per second) is the nucleation term, which must be defined according to physical laws. For example, a pragmatic approach originally developed by Oldfield[3, 27] was employed for both the grain nucleation during globular equiaxed solidification and the nucleation of the second phase droplets during decomposition in hypermonotectic alloys.

Mass transfer and grain (droplet) growth kinetics

As grains/droplets nucleate they start to grow. In the case of both the globular equiaxed solidification and the decomposition of the second phase droplets the morphology of the grains/droplets is simplified to be spherical. The average diameter d_q of the phase q is determined by its volume fraction α_q and the grain/droplet density n.

$$d_q = \left(6 \cdot \alpha_q \Big/ \pi \cdot n \right)^{\frac{1}{3}} . \tag{10}$$

In the case of globular equiaxed solidification the grain growth is determined by solute diffusion in front of a liquid-solid interface[18]. The solute element piles up (k<1) in front of the liquid-solid interface due to solute partitioning. The enriched solute can only be removed from the interface region to the bulk melt through diffusion. Therefore the concentration difference Δc between c_p^e (concentration in the melt at the interface) and c_p (concentration in the bulk melt) is taken as the driving force for solidification. Because a thermo-dynamic equilibrium at liquid-solid interface is assumed, c_p^e can be determined from the local temperature T according to the phase diagram. c_p is calculated from the solute conservation equation (7). In addition to the driving force term Δc, $\dot{m}_{pq}$ is proportional to the overall solid-liquid interface area. Thus, it depends on the grain density n and the grain surface area $\pi \cdot d_q^2$,

$$\dot{m}_{pq} = g_\alpha \cdot \Delta c \cdot (n \cdot \pi d_q^2) \cdot \rho_q \cdot \alpha_p . \tag{11}$$

The term α_p is the Avrami-factor. All other factors, which influence the solidification rate, are gathered in the empirical constant g_α (mm/s). g_α is here named as 'growth factor'.

The diffusion-controlled growth of a precipitation in a supersaturated matrix was described by Zener [29]. In the case of decomposition of secondary phase droplets in hypermonotectic alloys, the radius growth rate dR/dt of a droplet is governed by the difference between the far field concentration c_p and the concentration c_p^* of phase p (parent melt) at the interface, i.e. $\Delta c = c_p - c_p^*$. The solute partitioning at the interface is $\Delta c_d = c_q^* - c_p^* \approx c_q - c_p^*$, where c_q is the concentration of phase q (secondary phase droplet). Both c_p and c_q are obtained by solving the species conservation equation (7). D_p is the diffusion coefficient. If the droplet density n and an additional Avrami-factor α_p are considered, then the mass transfer rate $\dot{m}_{pq}$ (kg·m^{-3}·s^{-1}) from equation (11) is transformed to [23,26]

$$\dot{m}_{pq} = \frac{D_p}{d_q \cdot c_d} \cdot \Delta c \cdot \left(n \cdot \pi d_q^2\right) \cdot \rho_q \cdot \alpha_p . \tag{12}$$

Quantitative description of the macrosegregation

It is useful to recall that the cause of macrosegregation is the long-range advection of the alloy species due to the relative movement or flow of segregated liquid and solid during solidification[7]. In order to describe the macrosegregation quantitatively, an auxiliary quantity, i.e. the volume averaged solute concentration c_{mix}^i is defined:

$$c_{mix}^i = \sum_{q=1}^{\tilde{n}} c_q \rho_q \alpha_q \Big/ \sum_{q=1}^{\tilde{n}} \rho_q \alpha_q \tag{13}$$

The great advantage of this multi-phase model is that the concentration of each solute element i and each phase q can explicitly be solved with a species conservation equation (7).

Another key point in modelling the macrosegregation is the solute partitioning at the liquid-solid interface during solidification. For the solute partitioning, thermodynamics must be taken into account. Details about this procedure are described elsewhere [18-20].

Momentum exchange between different phases

The interphase momentum exchange includes the term due to mass transfer or phase change (e.g. solidification) and the term due to drag force. The momentum exchange rate due to solidification is described as follows. Assuming a mass transfer rate $\dot{m}_{pq}$ from phase p to q, a momentum (per unit mass and time) of $\vec{u}_p \cdot \dot{m}_{pq}$ will be transferred from phase p to q. In other words, the momentum of phase p will be reduced by an amount of $\vec{u}_p \cdot \dot{m}_{pq}$, and the same amount of momentum will be added to phase q.

The drag force term is based on the exchange coefficient K_{pq} in equation (3). In order to determine this coefficient, different cases must be distinguished. For the solidification problem, both stationary solid phase and moving solid are distinguished [18]. The drag force between the liquid phase and stationary solid phase is handled as for flow through porous medium, while the drag force between the liquid and free-moving grains is treated as for submerged objects. Correspondingly, different models (Kozeny-Karman and Blake-Kozeny) are used. In the case of hypermonotectic solidification, two liquid phases coexist before solidification starts. The morphology of the secondary liquid phase can be well expressed as dispersed droplets; therefore, the interaction between the droplets and the mother liquid is described as hydrodynamic resistance (Stokes force) [23, 26].

Marangoni force on the secondary liquid droplets

When a single droplet is placed in a melt having a temperature gradient ∇T, a thermo capillary convection in/around the droplet is induced. The temperature dependent surface energy forces the droplet surface from the hotter towards the colder pole. Consequently the droplet moves towards the hot region. This is called thermo capillary or Marangoni motion. Integration of the thermo-capillary force acting on the droplet surface is defined as Marangoni force $\bar{f}_M$. Based on the Stokes-Rybczynski-Hadamard approximation, Young et al.[30-32] have deduced $\bar{f}_M$ for a single droplet as

$$\bar{f}_M = \frac{\pi d_q^2}{(1+\mu_q/\mu_p)\cdot(2+k_q/k_p)} \cdot \frac{\partial\sigma}{\partial T} \cdot \nabla T . \qquad (14)$$

Further considering the droplet density n and equation (6), the volume averaged Marangoni force $\bar{F}_M$ ($N \cdot m^{-3}$) in equation (3) is expressed as

$$\bar{F}_M = \frac{6}{(1+\mu_q/\mu_p)\cdot(2+k_q/k_p)} \cdot \frac{f_q}{d_q} \cdot \frac{\partial\sigma}{\partial T} \cdot \nabla T . \qquad (15)$$

An empirical relationship for the Marangoni coefficient $\partial\sigma/\partial T$ is recommended [33-34].

$$\frac{\partial\sigma}{\partial T} = -1.26 \cdot \sigma_0 \cdot \frac{1}{T_c} \cdot \left(1 - T/T_c\right)^{0.26} , \qquad (16)$$

where σ_0 is determined experimentally.

Simulation Examples

Influence of phase separation on hypermonotectic solidification

For investigations on the solidification of hypermonotectic alloys a 2D square casting (90 x 90 mm^2) with the composition Al-10wt.%Bi has been simulated. The mold, remaining at a constant temperature of 290 K, is assumed to be filled instantaneously with a melt of 1065 K initial temperature. The heat exchange coefficient at the casting-mold interface is 750 $W/(m^2 \cdot K)$. The nucleation parameters for the liquid phase droplets are $n_{max} = 10^{13}$ m^{-3}, $\Delta T_N = 20$ K and $\Delta T_C = 8$ K. Further physical properties and modeling parameters are given in recent publications[23, 26].

Figure 2 shows a solidification sequence without (left hand side) and with (right hand side) gravity. There are 3 phases appearing in the phase diagram of this system during solidification: the primary liquid phase, the secondary liquid phase (Bi, solidification of this phase is ignored), and the solidified monotectic matrix[23].

In the case of zero gravity ($g = 0$) the Marangoni motion presents the only mechanism for the phase transport. Droplets of the secondary liquid phase start to nucleate and grow at the casting surface as the local temperature drops below the binodal point at 1062.2 K. The Marangoni force causes the droplets to move from the outer regions towards the casting center. The parent melt moves in reverse direction, because the space of the leaving droplets must be replaced by the parent melt. The droplet movement results in a depletion of the secondary liquid phase in the corners and outer regions, and an enrichment of the secondary liquid phase in the casting center.

As the casting further cools down to the monotectic point, monotectic reaction occurs, the velocity of the parent liquid phase vanishes and the droplets are entrapped in the monotectic matrix. When the solidification is finished the outer regions of the casting have a lower volume fraction of the secondary liquid phase and the center a higher. The spatial separation of the phases is directly responsible for the macrosegregation: $c_{mix} < 7.2\%$ Bi in the corners, $c_{mix} > 12\%$ Bi in the center. Both Marangoni motion and diffusion controlled growth contribute to an uneven droplet size distribution. A tendency of finer droplets in the outer regions and relatively

large droplets in the central region is predicted. Coagulation of droplets has not yet been considered in the recent model. This makes it difficult to directly compare the simulation results with experiments. However, the numerically predicted tendency of phase separation agrees qualitatively remarkably well with experiments performed by Walter in sounding rocket experiments with Al-Bi alloys[35].

Under normal terrestrial conditions (g = 9.8 m·s^{-2}) the droplets of the secondary liquid phase start to nucleate in the corners and along the walls, then grow and sink downwards along the vertical walls. As two liquid phases are coupled through the momentum exchange terms the parent melt is drawn by the sinking droplets, forming two vortices: one clockwise in the right half and one anti-clockwise in the left half of the casting. The convection currents in the parent melt are so strong that they in turn influence the movement and the distribution of the droplets. With the monotectic reaction the droplets are entrapped in the monotectic matrix and the phase and droplet size distributions remain unchanged afterwards.

The final solidification results show a depletion of the secondary liquid phase in the upper region and an enrichment of the secondary liquid phase in the central bottom region. A strong spatial separation of the phases leads to a strong macrosegregation: c_{mix} < 5% Bi in the upper region, c_{mix} > 25% Bi in the lower bottom region.

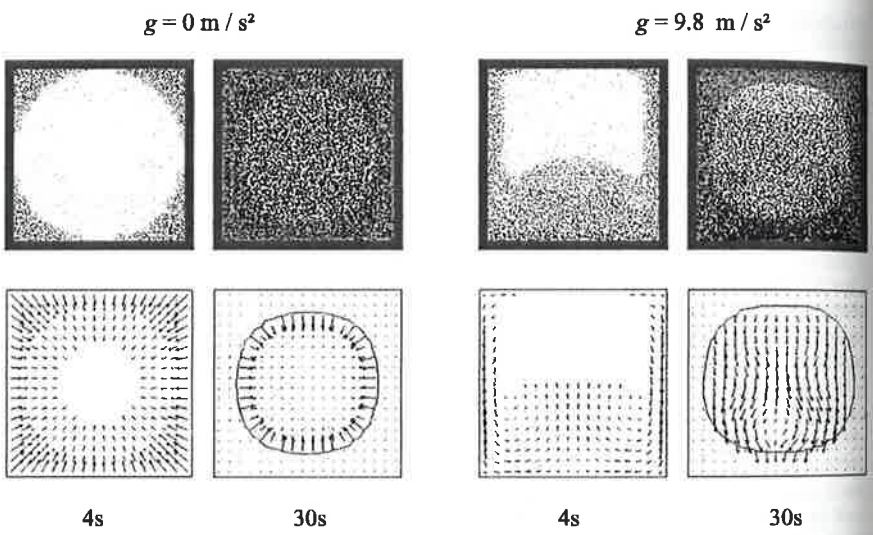

Figure 2: Solidification sequence of Al-10wt. %Bi without and with gravity. Bottom row: the velocity fields of the second phase droplets together with the monotectic front (T=925 K). Top row: the Bi droplet distribution. The black spheres represent the Bi droplets. The grey matrix means that the alloy has solidified, and the droplets are entrapped in the solid monotectic matrix. Both the droplet density and the diameter of the droplets, shown in this figure, have been linearly reduced and enlarged in order to make the droplet distribution better visible. Coagulation of droplets has not yet been considered.

The droplet distribution pattern is the direct outcome of melt convection and droplet transport. A tendency of small droplets in the upper region and large droplets in the lower bottom region is predicted. This predicted phase distribution agrees to a certain extent with experiment performed by Alkemper and Ratke in chill-cast Al-Bi alloys under terrestrial conditions[36].

We found that phase separation is an important requirement for modelling of the solidification of hypermonotectic alloys. Comparing zero and terrestrial gravity conditions we found that under normal terrestrial conditions, the gravity induced sedimentation dominates the spatial phase separation process. The results show a depletion of the secondary phase in the top region and enrichment of secondary phase in the middle bottom region. Under weightless condition, however, Marangoni force causes the secondary phase droplets to move from casting boundary regions towards the casting centre; furthermore it causes the parent melt to move in the reverse direction, which leads to a depletion of the secondary phase in the boundary regions and an enrichment of secondary phase in the casting centre.

Influence of phase separation on the formation of macrosegregation

As an example for the influence of phase separation on macrosegregation we present simulation results of an Al-4wt%Cu ingot casting in the figures 3 and 4. With Ti as grain finer, the solidification morphology of this alloy is assumed to be globular. Figure 3 illustrates the boundary conditions. The metallic die at a constant temperature of 290 K is assumed to be filled instantaneously with melt at 925 K. The heat exchange coefficient at the casting-mold interface is taken to be 750 W/(m^2 K). An open thermally isolated boundary condition at the casting top is applied, so that hot melt can constantly feed the casting. The nucleation parameters[21] are taken as n_{max}= 10^{14} m^{-3}, ΔT_N = 10 K, ΔT_σ = 4 K. Constant but different densities for both liquid and solid are used, hence the thermal-solute convection is ignored here. The phase transport phenomena in this model consider only solid sedimentation, sedimentation induced melt convection, and feeding flow. Further details of the problem description and the used physical properties can be found in the references[16-18].

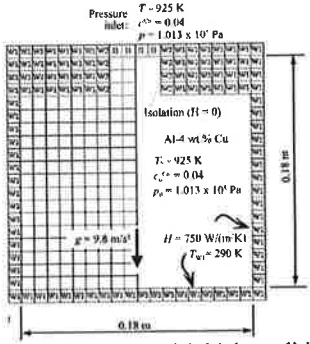

Figure 3. Geometry configuration, boundary and initial conditions of an ingot casting. The casting with an initial temperature of 925 K is poured into a mold with a constant temperature of 290 K.

Figure 4 illustrates the modeling results. In the initial stage of solidification, feeding flow caused by solidification shrinkage dominates the process. Nucleation and solidification start first in the four corners and subsequently along the mold walls. The grains nucleated directly on the wall do not move. With further solidification the grains, which do not directly adhere to the

mold walls, sink downwards. As the solid and the liquid are coupled through the momentum exchange term the melt is pulled by the sinking grains, forming two vortices: one clockwise in the right half and one anti-clockwise in the left half of the casting. Obviously at this stage of solidification the sedimentation and the sedimentation-induced melt convection dominate. Grain settlement occurs as the local fraction solid exceeds the packing limit ($\approx 64\%$). The grain movement leads to the accumulation of the solid phase in the lower corner and bottom regions. The grain settlement is responsible for the negative segregation in these areas (zones **A** and **D** in figure 4). Mechanisms for positive segregations are: (i) feeding of packed zones by segregated melt and (ii) squeezing out of segregated melt by settling grains[18]. The positive segregation zones **B** are caused by the first mechanism, while the zones **C**, which occur on the bulk melt, are caused by the second mechanism. The zones **C** move with the flow current and ascend towards the inner regions of the casting.

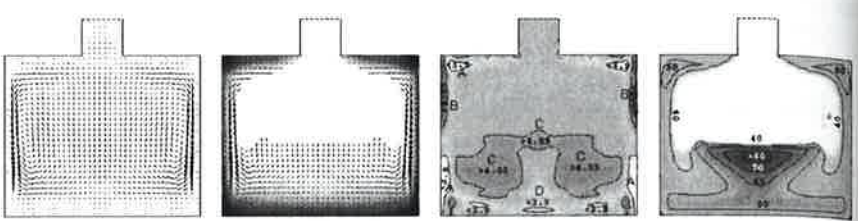

Figure 4: Solidification process (at 28s) of the Al-4wt%Cu ingot casting. The arrows of the velocities of the liquid $\bar{u}_{l,\max}$ and that of the solid $\bar{u}_{s,\max}$ are linearly scaled from zero to the maximum value given. The fraction solid α_s is shown together with the solid velocity. c_{mix} and d_s are shown with isolines together with 30 gray levels, with dark showing the highest value and bright the lowest.

A further example with the same alloy and a different geometry configuration is presented in Figures 5 and 6. The casting is assumed to be filled instantaneously and solidified in a closed die with constant temperature of 290 K. Sedimentation and sedimentation induced convection are considered with the Boussinesq approach, solidification shrinkage (feeding flow) and the thermal-solute convection have been ignored in this case. A steel chill located in the upper part of the die with initial temperature of 290 K is intentionally designed to stress the effect of grain sedimentation.

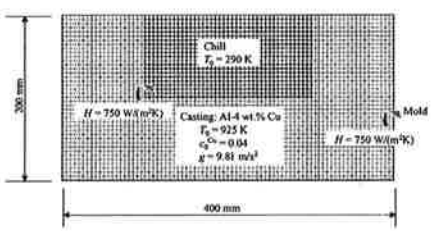

Figure 5. Geometry configuration, boundary and initial conditions of a die casting (Al-4wt%Cu). The metal with an initial temperature of 925 K instantaneously fills a die with a constant temperature of 290 K. During the solidification process the chill is allowed to heat up.

Grains, which nucleate around the steel chill and the die walls, sink downwards, inducing the special melt convection pattern shown in Figure 6. The sinking grains lead to the accumulation of the solid phase in the direct bottom region. With the same mechanism as mentioned above, the grains stop moving and settlement occurs when the local fraction solid exceeds the packing limit. The grain settlement in the bottom region is the direct reason for the negative segregation there. With proceeding solidification, the negative zone in the direct bottom region becomes wider and wider. The strongest negative segregations are found in the lower corners near the sidewall. This is easy to explain because grains, which nucleate along the sidewalls, sink downwards, thus strong settlement occurs in the lower corner regions.

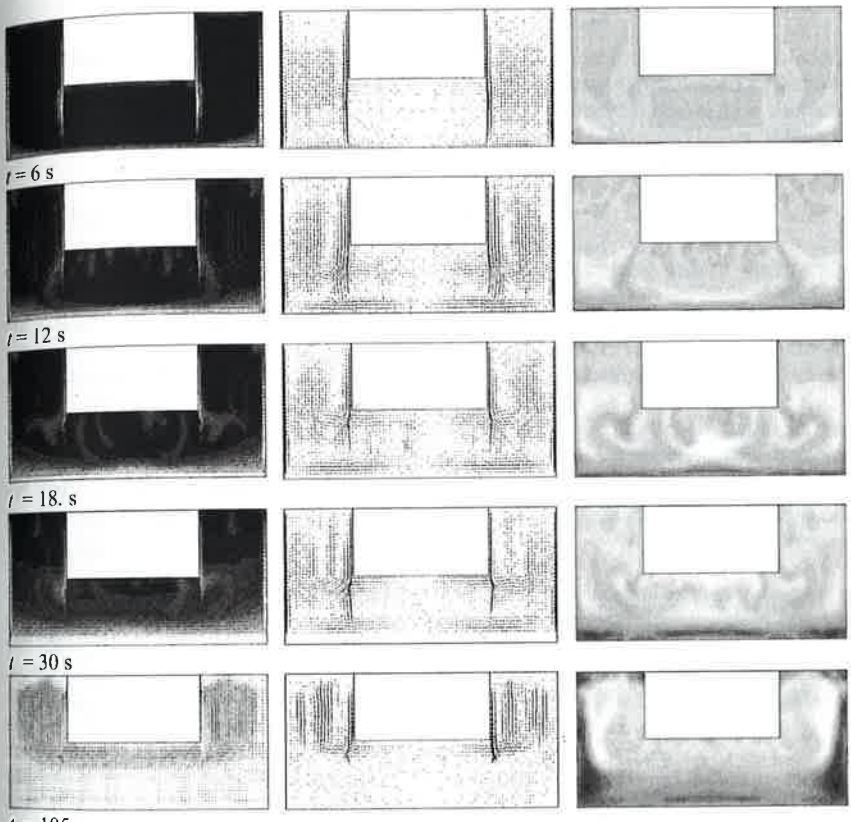

a) Volume fraction α_s and velocity $\bar{u}_s$ of solid phase

b) Velocity $\bar{u}_l$ of liquid phase

c) Macrosegregation c_{mix}

Figure 6. Sequence of macrosegregation formation. The arrows of each velocity field are continuously scaled starting from zero to the maximum value. The values of α_s are scaled equidistantly by 30 gray scales from zero (black) to 1.0 (white), and c_{mix} from 0.0315 (black) to 0.0485 (white).

In the example shown in figure 4, two mechanisms for the positive segregation are found: (i) feeding through segregated melt, and (ii) squeezing out of the segregated melt by the settling grains. In this simulation, however, the feeding flow has been ignored. The positive segregation caused by the mechanism of squeezing out of segregated melt is obvious. In the early stage of solidification (6 s), the grain settlement starts in the lower corner zones.
Accompanying to those grain settlement zones, positive segregations occur just close to them. Similarly, at about 12 s, a horizontal positive segregation zone just above the bottom settling zone starts to form. As these positive segregation zones forms in the bulk melt they are not stationary. They move with the flow current, ascend upwards, and form the last macrosegregation pattern shown in Figure 6(c).

Influence of phase separation on microstructures

A globular equiaxed solidification model was used to simulate macrostructure formation in an Al-4wt%Cu plate casting (Figure 7). Evaluation efforts were made by comparing the numerical predictions with a special experimental situation. Figure 8 shows the simulated grain size distribution in a section of an Al-4wt%Cu plate casting, compared with the experimental results.

The mold temperature was taken to be 573 K and the heat exchange coefficient at casting-mold interface to be 800 W/(m^2·K). A convection heat exchange boundary condition on the top surface of the casting was applied, the convection heat transfer coefficient was taken as 50 W/(m^2·K) and the environmental temperature as 283 K. Due to the high calculation cost the solidification simulation was carried out in 2D, i.e. the central cross section of the plate. A 3D mold filled simulation was carried out with the commercial software MAGMASOFT to predict the initial temperature distribution for the solidification simulation. The mold filling simulation predicted that the temperature in this central section after mold filling was relatively uniform; hence a constant temperature of 925 K is assumed. The initial mold temperature is 573 K. The nucleation parameters for the simulation are n_{max}= $1.5 \cdot 10^{12}$ m^{-3}, ΔT_N = 20 K, ΔT_σ = 8 K. The solidification shrinkage and the thermal-solute convection are ignored for this case, but sedimentation and sedimentation-induced convection were considered with the Boussinesq approach.

Sedimentation and sedimentation-induced flow currents, similar to the results shown in Figure 4, are also observed in the considered cross section of the plate casting: two vortices occur - one clockwise in the right part and one anticlockwise in the left part of the section. The numerically predicted grain size distribution across the section of the plate casting is shown in Figure 8 a). The fine grain size (~262 μm) at the bottom region is mainly due to the high nucleation rate in the initial stage, and partially due to the sedimentation. The largest grains (~390 μm) are predicted near the surface regions about 30~40 mm above the bottom. Those large grains are actually transported from the upper regions where they nucleated. They sink and grow. As they reach lower regions through a relatively long journey, they have grown to a large size. The relatively small grains predicted in the central region are due to the melt currents, which transport the fine grains from bottom regions upwards to the center. Comparing the results presented in figure 8b) and c), the grain size distribution in the real casting agree reasonably well with the numerical prediction. The absolute values for the grain sizes are somehow different between the numerical simulation and the experiment, but the distribution pattern is quite similar.

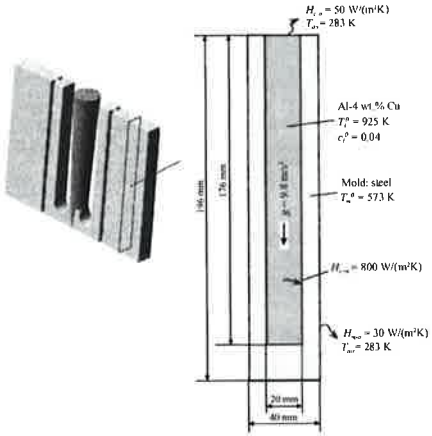

Figure 7. Geometry configuration, boundary and initial conditions of a plate ingot casting.

a) Simulated grain size distribution.

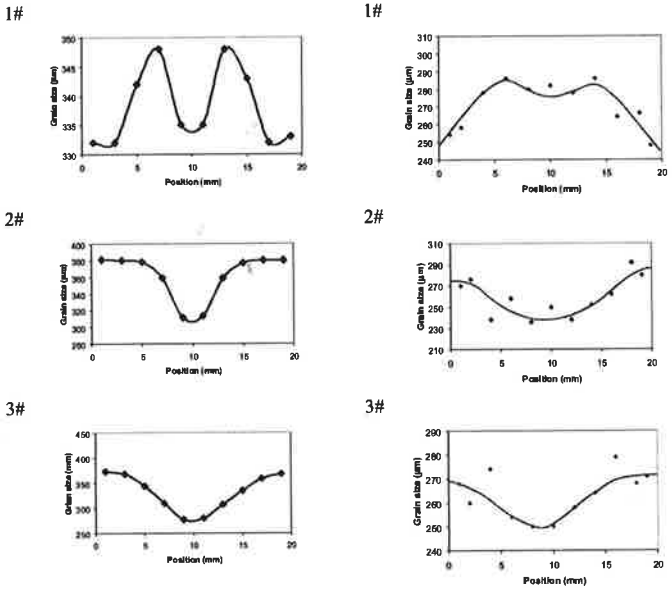

b) Simulated grain size distribution across the casting section at 3 different positions 1#, 2# and 3#.

c) The experimentally measured grain size distribution at the corresponding positions 1#, 2# and 3#.

Figure 8: Comparison of the numerically predicted grain size distribution to the experimentally measured results. The grain size distribution of the whole section is shown with 30 gray levels, with light showing the smallest grains (262 μm), and dark the largest (390 μm).

The casting section has also been EDX (energy dispersive X-ray) analyzed for macrosegregation. The experimentally measured data points are scattered, thus it is difficult to

fit the experimental data to the numerical results quantitatively. However, the measured result shows the same tendency as the simulation. There is a lower concentration in casting bottom region and a higher concentration in top region. Considering the simplifications made in the present model, we find the above agreement between the simulation and the experiment encouraging.

Summary

An Eulerian multiphase model was employed to investigate the influence of convection induced phase separation phenomena on the macrosegregation and macrostructure formation during solidification. Simulations of difference alloys with difference solidification behaviors have been presented, and the important findings are summarized in the following section.

- Marangoni force under weightless condition causes the L_2 droplets to move from casting boundary regions towards the casting centre, and the parent melt L_1 to move in reverse direction, leading to depletion of L_2 phase in the boundary regions and enrichment of L_2 phase in the casting center.
- Although both gravity-induced sedimentation and Marangoni motion occur under normal terrestrial condition, the gravity induced sedimentation dominates the spatial phase separation process. The final results show a depletion of the L_2 phase in the top region and an enrichment of the L_2 phase in the middle bottom region.
- Coagulation of the droplets has not yet been implemented in the model. Thus a precise comparison of the simulation results with the experiments is not yet possible, however the numerically predicted Bi droplet distributions in hypermonotectic alloy (Al-10wt%Bi) under both normal terrestrial and weightless conditions agree qualitatively with the ground experiments performed by Alkemper and Ratke [36], and the sounding rocket experiments performed by Walter [35], respectively.
- The convection-induced phase separation results directly in macrosegregation. Grain settlement is responsible for the negative segregation. In case of globular equiaxed solidification, negative segregations are found, for example, near lower corners of the casting and at the middle bottom region, where sedimentation frequently occurs. Positive macrosegregation forms for two reasons (i) feed of segregated melt to packed zones; (ii) squeezing out of segregated melt by settling grains. Areas of positive segregation caused by the second reason may not be stationary and thus move during solidification with the melt flow, while those caused by the first reason do not move.
- The macrostructure distributions in the case of globular equiaxed solidification are the outcome of both growth kinetics and phase separation (free moving grains). The simulation results on a plate casting (Al-4wt%Cu) have successfully explained the experimentally observed grain size distributions.

References:

1. C. Beckermann and R. Viskanta, *Appl. Mech. Rev.* Vol 46, No. 1, 1993, pp.1
2. C. Beckermann and C.Y. Wang, *JOM*, Vol 46, 1994, pp. 42
3. M. Rappaz, *Intern. Mater. Rev.* Vol 34, 1989, pp.93
4. V.R. Voller and F. Porte-Agel, *J. Computational Phys.*, 2001, pp.0324
5. A.Ohno, *Solidification-The Separation Theory and its Practical Applications*, (Berlin: Springer-Verlag, 1987)
6. C. Beckermann, *JOM*, Vol 49, 1997, pp. 13
7. C. Beckermann, *Intern. Mater. Rev.*, Vol 47, 2002, pp. 243
8. J. Ni, C. Beckermann, *Metall. Trans.*, Vol 22B, 1991, pp. 349

9. C.Y. Wang, C. Beckermann, *Metall. Mater. Trans.*, Vol 27A, 1996, pp. 2754
10. C.Y. Wang, C. Beckermann, *Metall. Mater. Trans.*, Vol 27A, 1996, pp. 2765
11. C.Y. Wang, C. Beckermann, *Metall. Mater. Trans.*, Vol 27A, 1996, pp. 2784
12. A.V. Reddy, C. Beckermann, *Metall. Mater. Trans.* Vol 28B, 1997, pp.479
13. J. Ni, F.P. Incropera, *Inter. J. Heat Mass Transfer*, Vol 38, 1995, pp. 1271
14. J. Ni, F.P. Incropera, *Inter. J. Heat Mass Transfer*, Vol 38, 1995, pp. 1285
15. O. Nielsen, A. Appolaire, H. Combeau, A. Mo, *Metall. Mater. Trans*, Vol 32A, 2001, pp.2049
16. A. Ludwig, G. Ehlen, M. Pelzer, P.R. Sahm, *9th Int. Conf. on McWASP-IX*, eds.: P.R. Sahm et al, Aachen , 2000, pp. 175
17. Ludwig, M. Wu, G. Ehlen, P.R. Sahm, *Materials Week Proceedings*, Munich, 2000, accessible via www.materialsweek.org
18. A. Ludwig, M. Wu, Metall. *Mater. Trans.* Vol 33A , 2002, pp. 3673
19. A. Ludwig, M. Wu, M. Fehlbier, C. Afrath, A. Bührig-Polaczek, *10th Int. Conf. on McWASP-X*, eds. D. Stefanescu et al, Florida, 2003, pp191
20. A. Ludwig, M. Wu: *Tagungsband zur 8. Werkstofftagung*, TU-Graz, ed.: H. Cerjak, 2003, pp. 11
21. M. Wu, A. Ludwig, *Adv. Eng. Mater.*, vol. 5, 2003, pp. 62
22. M. Wu, A. Ludwig, A. Bührig-Polaczek, M. Fehlbier, P.R. Sahm, *Int. J. Heat Mass Transfer.*, Vol 46, 2003, pp. 2819-2832
23. M. Wu, A. Ludwig, L. Ratke, *Modell. Simul. Mater. Sci. Eng.*, Vol 11, 2003, pp. 755-769
24. M. Wu, A. Ludwig, L. Ratke, *10th Int. Conf. on McWASP-X*, eds.: D. Stefanescu et al, Florida, 2003, pp. 141-148
25. M. Wu, A. Ludwig, P.R. Sahm, A. Bührig-Polaczek, *10th Int. Conf. on McWASP-X*, eds.: D. Stefanescu et al, Florida, 2003, pp. 261-268
26. M. Wu, A. Ludwig, L. Ratke: *Metall. Mater. Trans. A*, Vol. 34, 2003, pp 3009.
27. W. Oldfield, *Trans. ASM*, Vol. 59, 1966, pp. 945-961
28. FLUENT 4.5 Manual, Fluent Incorporated Centerra Resource Park, 10 Carvendish Court, Lebanon, NH 03766, 1998.
29. C. Zener, *J. Appl. Phys.*, Vol 20, 1949, pp. 950-953
30. N. O. Young, J.S. Goldstein, M.J. Block, *J. Fluid Mech.*, Vol.6, 1959, pp. 350-356
31. W. Günter "*Über die Dynamik von Fluidpartikeln aufgrund des Marangoni-Effektes*" (Düsseldorf: VD-Verlag, 1993)
32. M.G. Velraade „*Materials and Fluids Under Low Gravity*" ed.: L. Ratke (Berlin: Springer Verlag, 1995), pp- 283-298
33. L. Ratke, S. Diefenbach, *Mater: Sci. Eng.*, vol. 15, 1995, pp. 263-347
34. S. Diefenbach „*Modellierung der Gefügeentwicklung von Monotekta*" (Bochum: PhD Thesis, 1993)
35. H. U. Walter, in Järva Krog (eds.), *Proc. RIT/ESA/SSC Workshop*, ESA SP 219, Noordwijk, Sweden, 1984, pp. 47-64
36. J. Alkemper, L. Ratke, *Z. Metall.* , Vol.85, 1994, pp. 365-371